Supporting Information

Multifunctional metal-phosphide-based electrocatalysts for highly efficient solar hydrogen production integrated devices

Jin−Tao Ren [a], Lei Chen [a], Lei Wang [a], Xin−Lian Song [a], Qing−Hui Kong [a], and Zhong−Yong Yuan [a,b,*]

[a] *National Institute for Advanced Materials, School of Materials Science and Engineering, Smart Sensing Interdisciplinary Science Center, Nankai University, Tianjin 300350, China.*

[b] *Key Laboratory of Advanced Energy Materials Chemistry (Ministry of Education), Nankai University, Tianjin 300071, China.*

*Corresponding author. E-mail: zyyuan@nankai.edu.cn (Z.−Y. Yuan).

1. Supplementary experimental section

1.1. Synthesis for PANI–ATMP/CC and PANI/CC

First, a piece of carbon cloth (CC) was sonicated with acetone, hydrochloric acid, and deionized water for 30 min, respectively. Then, CC was dried at 60 °C. The PANI nanorod arrays were synthesized by a modified electrodeposition method. In the typical synthesis, two pieces of treated CC are employed as working electrode and counter electrode, respectively, and Ag/AgCl electrode was used as reference electrode. The electrolyte was fabricated by adding 10 mL of amino trimethylene phosphonic acid (ATMP) solution (50 wt%) into 90 mL of deionized water, and then adding 4.5 mL of aniline to form uniform solution. The electrodeposition was conducted at 0.8 V vs.Ag/AgCl for 10 min, the ATMP–modified PANI nanorods arrays supported on CC were prepared, and denoted as PANI–ATMP/CC. For the synthesis of PANI/CC, the ATMP solution was replaced by concentrated hydrochloric acid, and the other steps are similar to that of PANI–ATMP/CC, and the resulted materials were labeled as PANI/CC.

1.2. Synthesis for NiFe LDH on PANI nanorod arrays

The prepared PANI–ATMP/CC or PANI/CC was placed in a 150 mL solution of 3 mM $Ni(NO_3)_2$ with 3 mM $Fe(NO_3)_3$ as the working electrode, the Pt mesh as the counter electrode, and Ag/AgCl as the reference. The working electrode was held at –1.0 V vs. Ag/AgCl for 10 minutes and a hydroxide layer was formed. And the resultant samples was denoted as LDH PANI–ATMP/CC and LDH PANI/CC.

1.3. Synthesis for FeNiP@p–NPCF/CC, NiFe@NCF/CC, p–NPCF/CC, and NCF/CC

The LDH PANI–ATMP/CC, LDH PANI/CC, PANI–ATMP/CC, and PANI/CC were heated at 900 °C for 2 h under Ar atmosphere to form FeNiP@p–NPCF/CC, NiFe@NCF/CC, p–NPCF/CC, and NCF/CC, respectively.

1.4. Synthesis of Pt/C–RuO2/CC

0.5 mg of Pt/C (20 wt%) and 0.5 mg of RuO_2 were added into 0.2 mL of Nafion solution (0.1% wt) to form ink, then the ink is evenly dripped onto the carbon cloth (1 cm $\times$ 1 cm). Finally, dried in a vacuum oven. The Pt/C–RuO_2/CC was obtained.

1.5. Physical characterization

The scanning electron microscope (SEM) images were obtained by Jeol JSM–7800F. Transmission electron microscopy (TEM) and high–resolution TEM (HRTEM) images were determined by using a Jeol JEM–2800 system. X–ray diffraction (XRD) data was acquired on a Rigaku Smart Lab 3kW Diffraction System with a Cu $K\alpha$ radiation (λ=0.154178 nm). X–ray photoelectron spectroscopy (XPS) measurements were performed with a Thermo Scientific ESCALAB 250Xi with Al $K\alpha$ as the excitation source. For SEM, XRD, and XPS characterizations, the as–prepared samples on carbon cloth was directly measured without further treatment. For TEM characterization, a piece of carbon cloth with sample was sonicated in ethanol for 10 min to get the dispersion. Then a small drop of the dispersion was dropped onto a copper grid to be viewed under the microscope. Inductively coupled plasma optical emission spectrometer (ICP–OES) was carried out on a Thermo Fisher

iCAP7400 equipped with an Auto sampler Injector. For ICP–OES, a carbon cloth with sample was immersed in newly–prepared aqua regia overnight. Then plenty of deionized water was added to dilute the aqua regia and carefully boiled to drive HCl away from the solution. After re–adding water and boiling for several times, the left solution was carefully collected and diluted to suitable concentration for measurement. N_2 adsorption–desorption isotherms were measured on a Quantachrome Autosorb-1 sorption analyzer at liquid nitrogen temperature (77 K). Specific surface areas were obtained by using the multi–point Brunauer–Emmett–Teller (BET) method. Fourier transform infrared (FT-IR) spectra were measured on a Bruker VECTOR 22 spectrometer with KBr pellet technique. Thermogravimetry (TG) was formed using a TA SDT Q600 instrument at a heating rate of 5 ℃ min^{-1} using α-Al_2O_3 as the reference.

1.6. Electrochemical measurement

The electrochemical measurements were conducted using a CHI 760E electrochemical workstation (Chenhua, Shanghai) in a typical three electrodes setup, with the as–prepared samples on CC as the working electrode, graphite rod as the counter electrode and an Ag/AgCl electrode as the reference electrode in the presence of 1.0 M KOH electrolyte. All the potentials in the text, if not specified, were recorded relative to the reversible hydrogen electrode (vs. RHE). The polarization curves were conducted with a scan rate of 5 mV s^{-1} with iR–compensation. Cyclic voltammetry (CV) curves in double layer capacitance (C_{dl}) determination were measured in a potential window nearly without Faradaic process at different scan rates of 10–50 mV s^{-1}. The plot of current density at set overpotential against scan rate has a linear relationship and its slope is the C_{dl}. The chronopotentiometric curve was performed with the stable current density. The Faradaic efficiency was calculated by comparing the amount of gas theoretically calculated and experimentally measured. The gas experimentally generated from the water splitting was collected by water–gas displacing method. The theoretical amount of H_2 and O_2 were calculated by applying the Faraday law.

All the potentials for HER and OER in this work were calibrated with 100% iR compensation to account for the voltage drop between the reference and working electrodes within the cell, if not specially stated, and R was determined by Electrochemical Impedance Spectroscopy (EIS). In the three-electrode tests of HER and OER, the solution resistance (R) value is about 1.2 and 1.1 Ω, respectively. However, the ORR polarization curves were presented without iR compensation.

All three-electrode LSV curves were manually iR-corrected according to the equation:

$$E_{corrected} = E_{measured} - iR$$

where the R is the solution resistance according to EIS test.

In order to evaluate ORR performance more clearly and elucidate the reaction mechanism of ORR process on catalysts, corresponding rotating disk electrode (RDE) and rotating ring disk electrode (RRDE) measurements were further carried out, with the RDE or RRDE coated with catalyst ink as the working electrode. As for the preparation of catalyst ink, 5 mg of FeNiP@p-NPCF powder catalyst was peeled off from self-supported FeNiP@p-NPCF/CC, which was then dispersed in a solution consisting of 800 μL isopropanol, 180 μL distilled water and 20 μL Nafion (5 wt%), finally forming a homogeneous catalyst ink through sonication. Then, 10 μL of the catalyst ink was dropped onto the

polished glassy carbon electrode and dried at room temperature, with the loading mass of 0.255 mg cm^{-2}.

To investigate the adsorption ability of the synthesized electrode to oxygen, the prepared electrodes were firstly immersed in O_2 saturated solutions to make their exposed active sites filled with adsorbed O_2. Then, the electrode were transferred to N_2 saturated solution and N_2 filled electrolytic tank. Chronoamperometry was conducted at 0.80 V vs.RHE to consume adsorbed O_2 in the free–standing electrodes. The amount of adsorbed O_2 can be evaluated by the quantity of electricity. Additionally, cyclic voltammetry was measured in the potential range of 0 – 1.2 V at various scan rates in O_2 saturated solution. The oxygen diffusion coefficient can be calculated by linear fitting current peaks to square roots of scan rates.

The number of active sites was measured by cyclic voltammetry (CV) curve in phosphate buffered saline solution (PBS, pH =7) according to the previous reports. Specifically, the n values of the as-prepared catalysts were calculated by the following formula:

$$n = Q/2F = It/2F = IV/2Fv$$

where Q is the voltammetric charge, F represents the Faraday constant (C mol^{-1}), I stands for the current (A), t is the time (s), V refers to the voltage (V) and v is the adopted scanning rate (V s^{-1}). As such, the TOF was calculated by the following equation:

$$TOF = I/mnF$$

where I is the current recorded during the LSV tests in 1 M KOH with the unit of A, F stands for the Faraday constant of 96,485 C mol^{-1}, n represents the number of active sites (mol) and m represents the number of electrons consumed to form one H_2 or O_2 molecule from the water. Therefore, the m values for hydrogen evolution reaction and oxygen evolution reaction are 2 and 4, respectively.

1.7. Fabrication of liquid zinc–air batteries

The liquid zinc–air battery is constructed by FeNiP@p–NPCF/CC air–electrode, alkaline electrolyte and polished Zn plate anode. The electrolyte is 6.0 M KOH +0.2 M Zn(CH$_3$COO)$_2$ mixed solution. The performance of FeNiP@p–NPCF/CC based liquid Zinc–air battery is evaluated by using a LAND–CT2001A testing equipment.

The specific capacity (mAh g^{-1}) was calculated according to the equation:

(current × ervice hours) / (weight of consumed zinc)

The energy density (mWh g^{-1}) is calculated according to the equation:

(current × service hours × average discharge voltage) / (weight of consumed zinc)

1.8. Self–made water–splitting unit

A home–made water–splitting unit is assembled by using FeNiP@p–NPCF/CC as anode electrode and cathode electrode, and driven by liquid zinc–air batteries. The obtained O_2 and H_2 flow along the gas duct and are collected by drainage collection method.

1.9. Assembly of solar-driven H$_2$ production

The solar-powered hydrogen production system was built by connecting such electrolyzer to a commercial silicon solar cell (2 W) powered by natural sunlight in day (from 8:00 AM to 18:00 PM), while, besides other time in night, the electrolyzer was derived by two aqueous zinc-air batteries in

series. The Keithley 2450 source meter and multimeter were used to measure the current in the circuit.

1.10. Density functional theory calculations

DFT-based first-principles calculations were conducted using the projector augmented wave (PAW) method. The exchangecorrelation functional is treated within the generalized gradient approximation (GGA) of Perdew-Burke-Ernzerhof (PBE). The energy cutoff for the plane wave basis expansion was 450 eV and the force on each atom less than 0.03 eV/Å was set for convergence criterion of geometry relaxation. Partial occupancies of the Kohn-Sham orbitals were allowed to use the Gaussian smearing method with a width of 0.05 eV. The Brillourin zone was sampled with Monkhorst mesh $2 \times 2 \times 1$ for all the computational process. The self-consistent calculations apply a convergence energy threshold of 10^{-5} eV and a 15 Å vacuum space along the z direction was used to avoid the interaction of two neighboring atoms.

2. Supplementary Figures
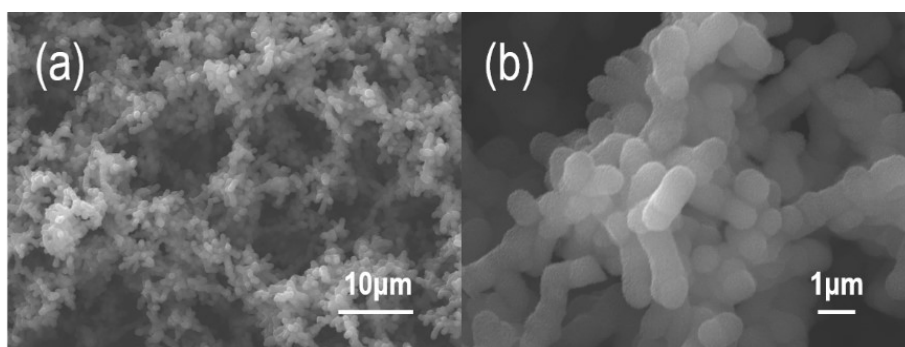
Fig. S1. SEM images of PANI-ATMP/CC.
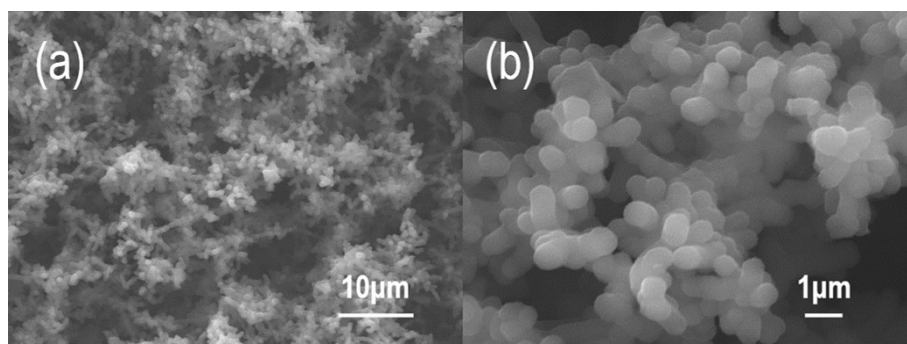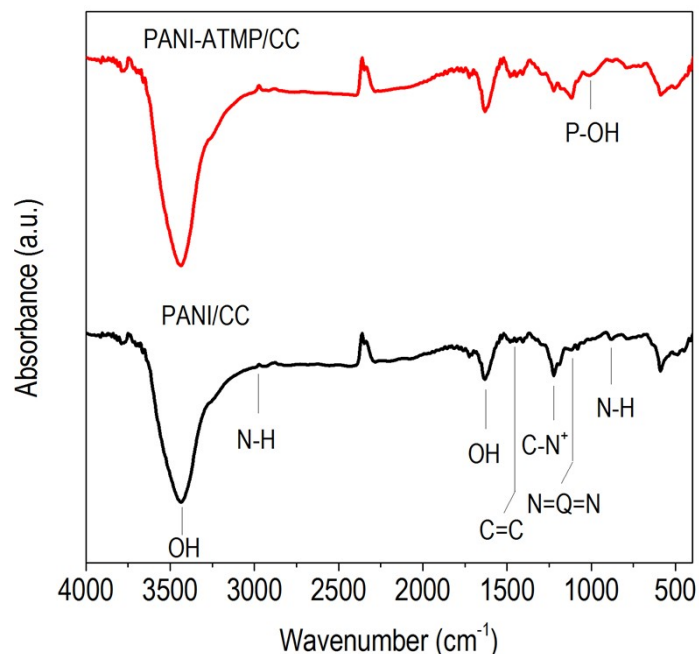

Fig. S2. SEM images of PANI/CC.

Fig. S3. FTIR spectra of PANI-ATMP/CC and PANI/CC. FTIR spectroscopy is a technique to examine the status of the bonds and microstructure of the materials. As the synthesized PANI/CC, the peak formed at a frequency of 886 cm^{-1} represents the N–H flexural bonds of the functional groups participating in hydrogen bonds.[1] Meanwhile, the characteristic bands at 1224 cm^{-1} attributed to the C-N^{+} stretching of polaron and 1119 cm^{-1} resulting from the N=Q=N (Q represent quinoid ring) stretching.[2, 3] The peaks at wavenumbers 1469 cm^{-1} and 1422 cm^{-1} represent the presence of C=C stretching of the quinoid (Q) and benzoid (B) rings, respectively.[4] Moreover, the peak at wavenumber 2978 cm^{-1} give sign to the presence of N-H stretching of the secondary amine.[5] The strong, broad band at 3427 cm^{-1} and the sharp band at 1632 cm^{-1} correspond to the surface-adsorbed water and hydroxyl groups. However, for the synthesized PANI-ATMP/CC materials, besides the typical peaks ascbribed to PANI, the evident vibration band at 991 cm^{-1} is attributed to P–OH in ATMP.[6] Therefore, those FTIR results demonstrate the successful introduction of ATMP molecules into PANI chains on the basis of acid–base interaction.[7]
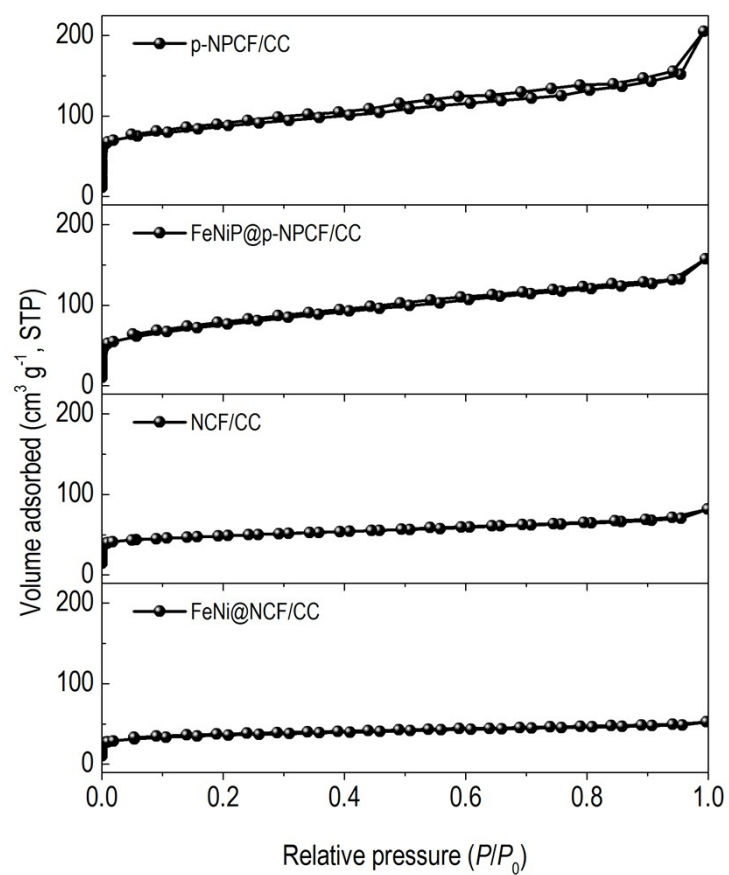
Fig. S4. N$_2$ sorption isotherms of as-prepared catalysts.
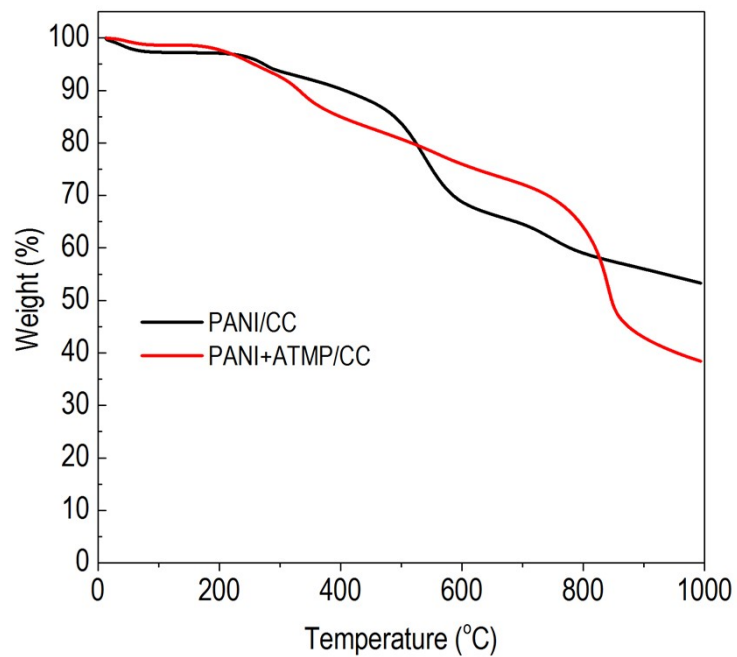
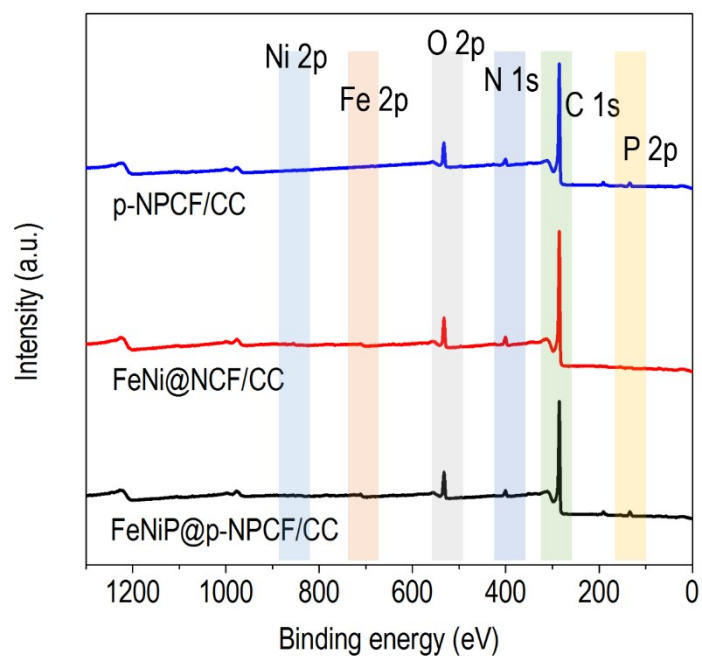**Fig. S5**. TGA curves of the synthesized materials.

Fig. S6. Full-range XPS spectra of NiFeP@p-NPCF/CC, NiFe@NCF/CC, and p-NPCF/CC.
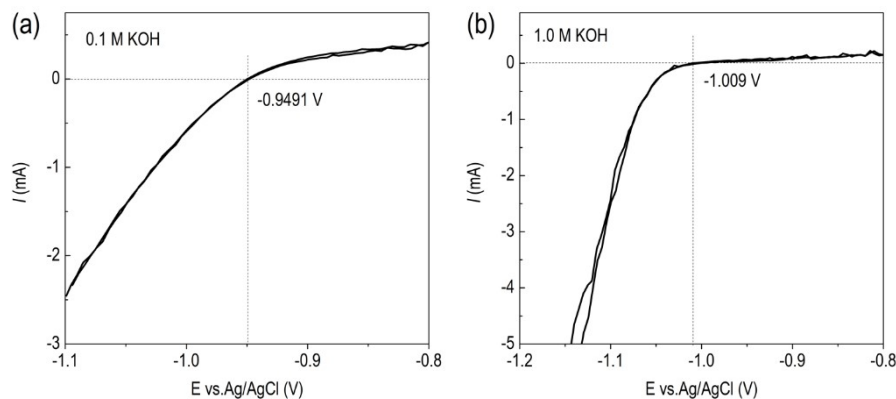
Fig. S7. Reference electrode calibration in 0.1 M KOH (a) and 1.0 M KOH (b).

Reference electrode calibration: 0.1 M KOH and 1.0 M KOH electrolyte solution were purged with hydrogen gas for 30 min prior the measurements. Two Pt nets, and Ag/AgCl electrode were used as counter, working, and reference electrodes, respectively. Cyclic voltammetry (CV) was obtained at a scan rate of 5 mV s^{-1} in the potential region of -0.7 to -1.1 V (*vs*. Ag/AgCl). Thermodynamic potential of the hydrogen electrode reaction were taken at the zero current crossing the average of the two potentials. Therefore, the results indicate that $E_{(Ag/AgCl)}$ is lower than $E_{(RHE)}$ by 0.9491 V and 1.009 V in 0.1 M KOH (pH=12.8) and 1.0 M KOH (pH=13.6), respectively.
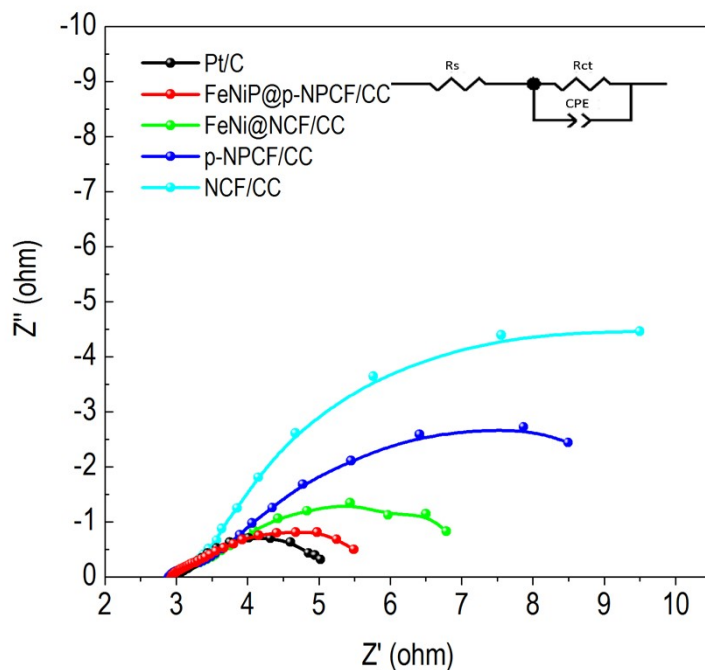

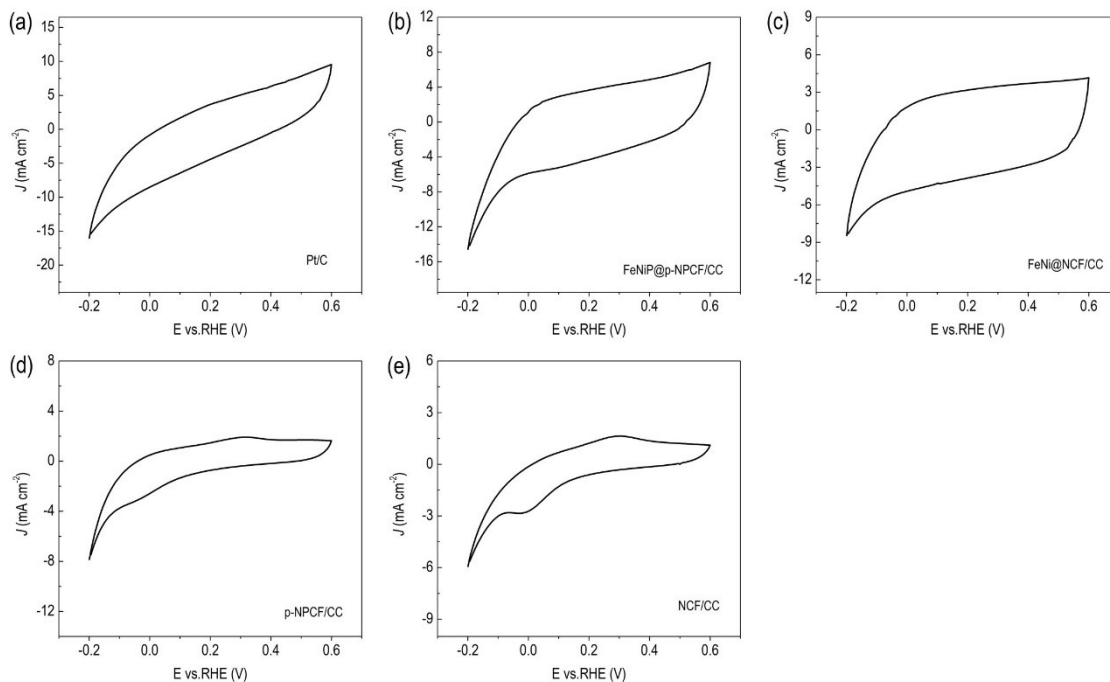**Fig. S8**. Nyquist plots of the fabricated catalysts.

Fig. S9. Cyclic voltammogram (CV) curves (a) Pt/C, (b) FeNiP@p-NPCF/CC, (c) FeNi@NCF/CC, (d) p-NPCF/CC, and (e) NCF/CC electrocatalysts measured in 1 M PBS (pH = 7) electrolyte at a scan rate of 50 mV s^{-1}.
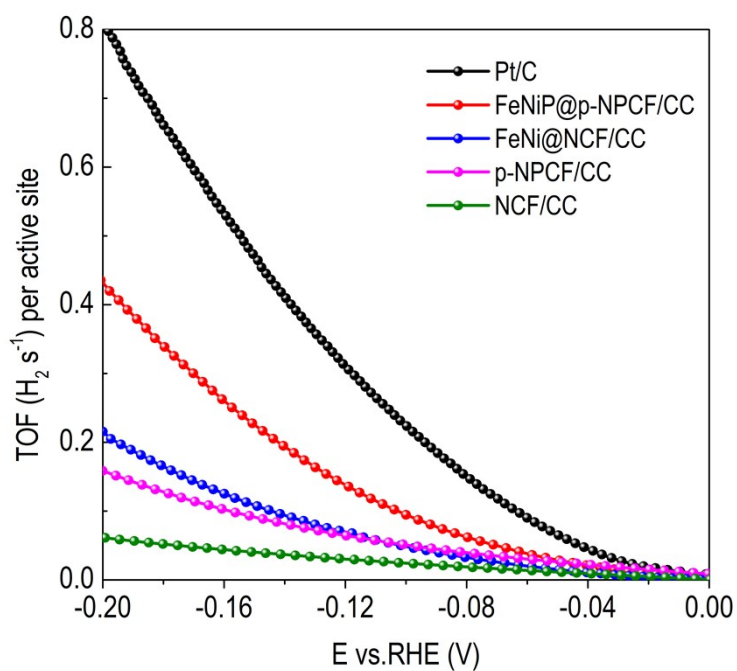

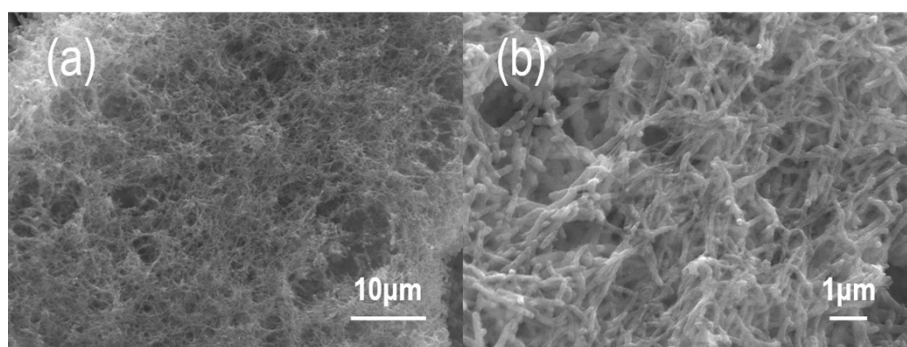**Fig. S10**. Calculated H$_2$ TOF values for Pt/C, FeNiP@p-NPCF/CC, FeNi@NCF/CC, p-NPCF/CC, and NCF/CC.

Fig. S11. SEM images of FeNiP@p–NPCF/CC after HER test.
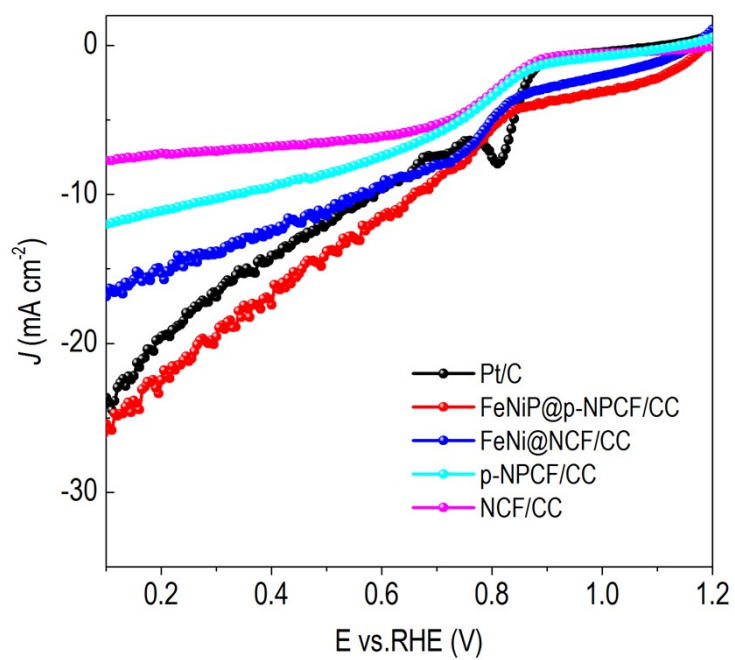

Fig. S12. ORR polarization curves of the fabricated catalysts.
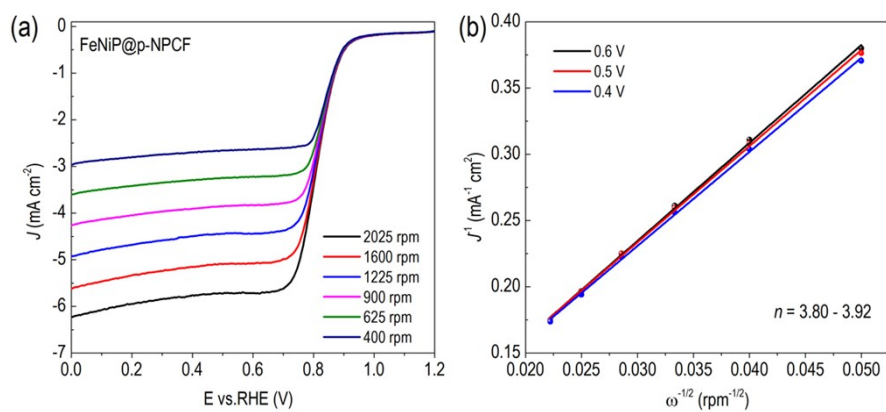
Fig. S13. (a) LSV curves of the NiFeP@p-NPCF under different scan rates. (b) K-L plots.
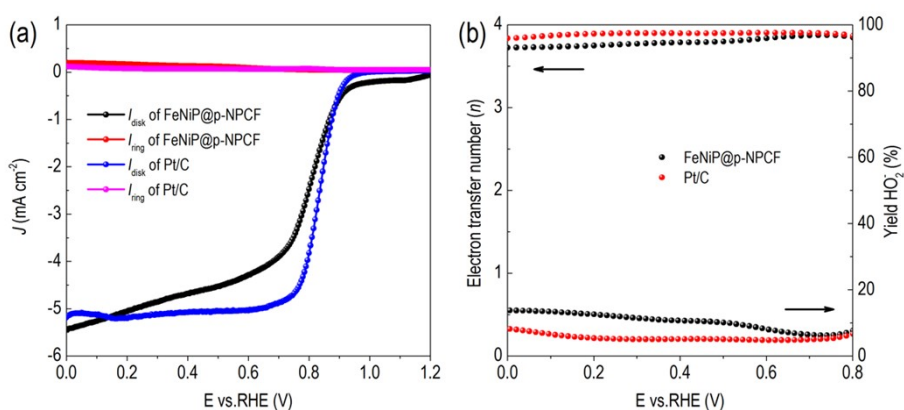

Fig. S14. (a) RRDE curves of the NiFeP@p-NPCF and Pt/C. (b) Determined n and H_2O_2 yield of the NiFeP@p-NPCF and Pt/C.
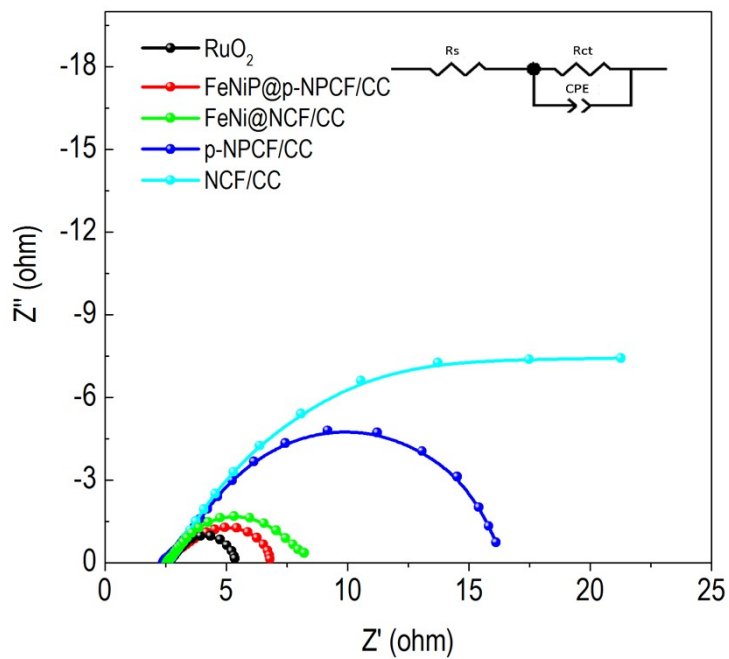
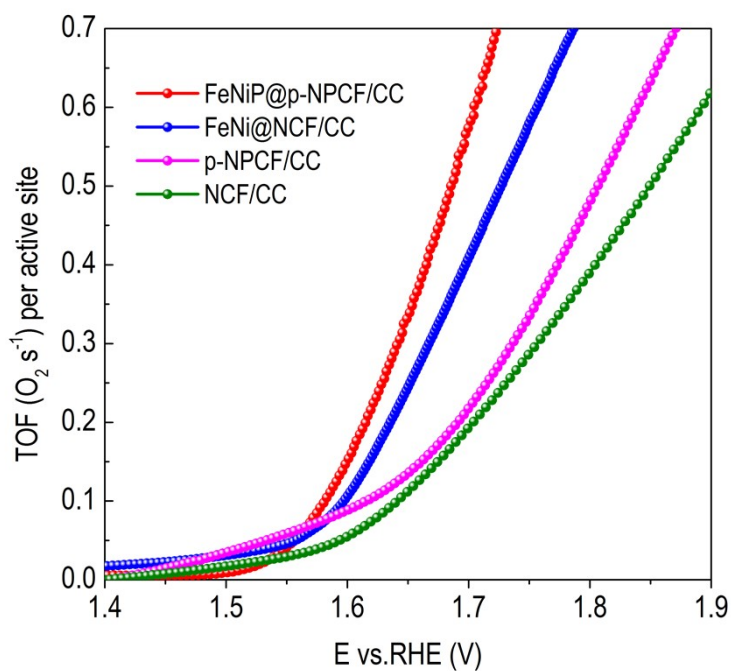**Fig. S15**. Nyquist plots of the fabricated catalysts.

Fig. S16. Calculated O_2 TOF values for FeNiP@p-NPCF/CC, FeNi@NCF/CC, p-NPCF/CC, and NCF/CC.
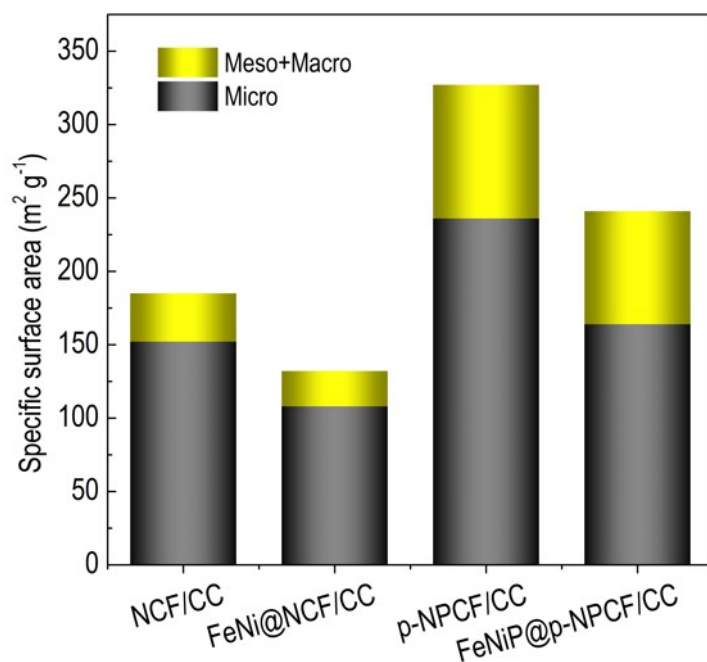
Fig. S17. Specific surface area of as–fabricated catalysts.
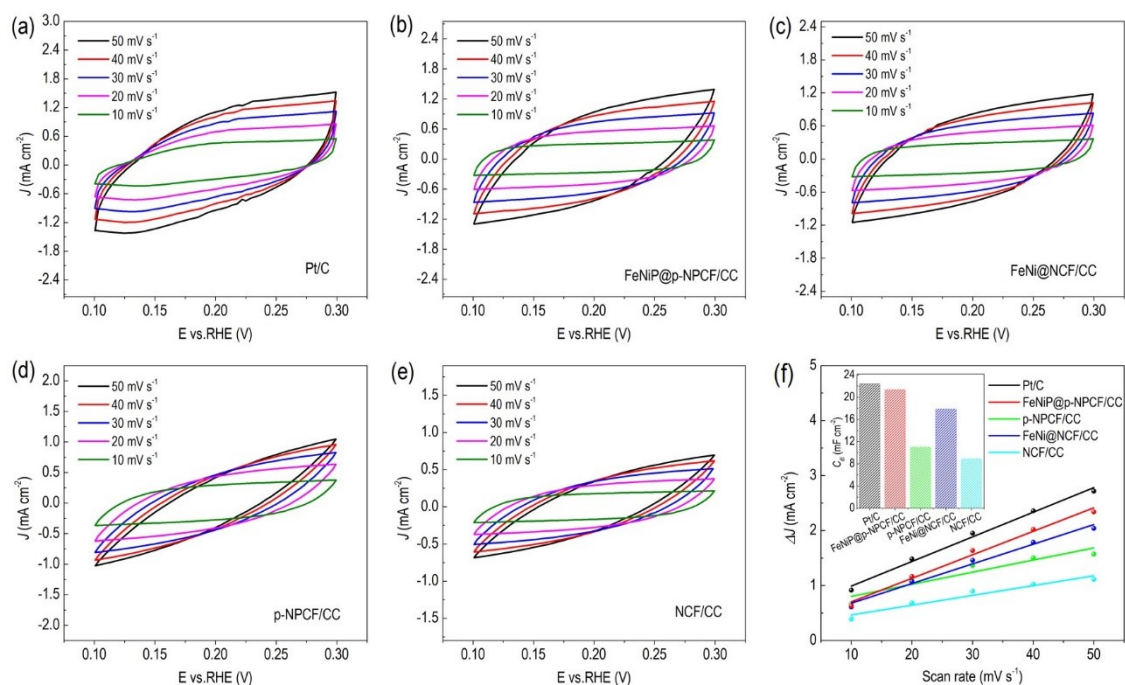
Fig. S18. (a-e) CV curves of the fabricated catalysts under different scans. (f) Determined double–layer capacitance (C_{dl}) from CV curves.
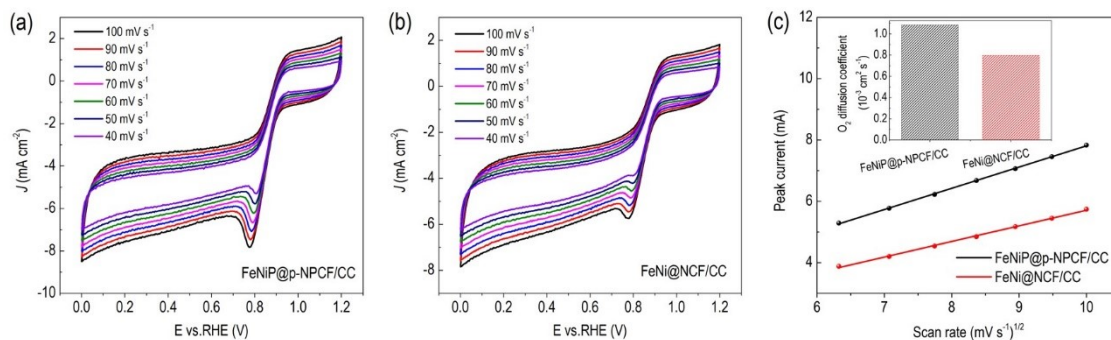
Fig. S19. (a,b) CV curves of the fabricated catalysts in O_2-saturated 0.1 M KOH. (c) Linear fitting between current peaks and square roots of scan rates, and inset is diffusion coefficient of oxygen in catalysts.
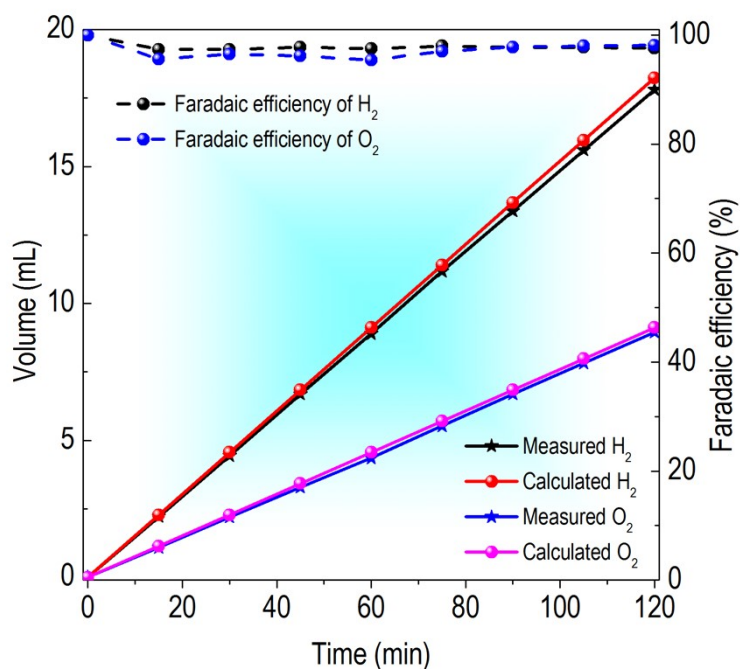
Fig. S20. Experimental and theoretical volumes of H_2 and O_2 by the FeNiP@p-NPCF/CC electrode at the current density of 20 mA cm^{-2}. And the corresponding Faradaic efficiency for H_2 and O_2.
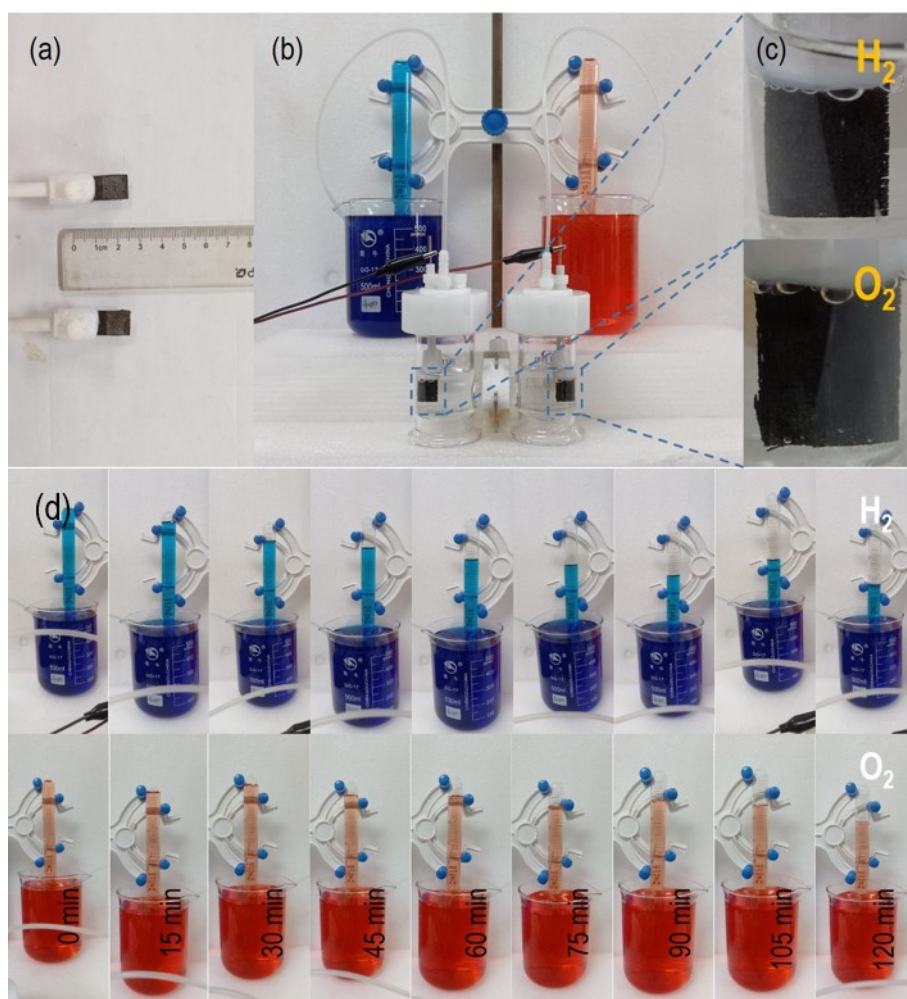
Fig. S21. (a) The prepared self-supporting electrode, and the white material above the electrode was hot melt adhesive coating used to fill the carbon cloth and prevent electrolyte from wicking upward out of the solution. (b) Digital image of the electrodes in the two-electrode electrolyzer, and the corresponding water displacement instrument. (c) The detail H_2 and O_2 generation on the cathode and anode, respectively. (d) Enlarged digital images of the measuring gas quantity generated in 120 min.
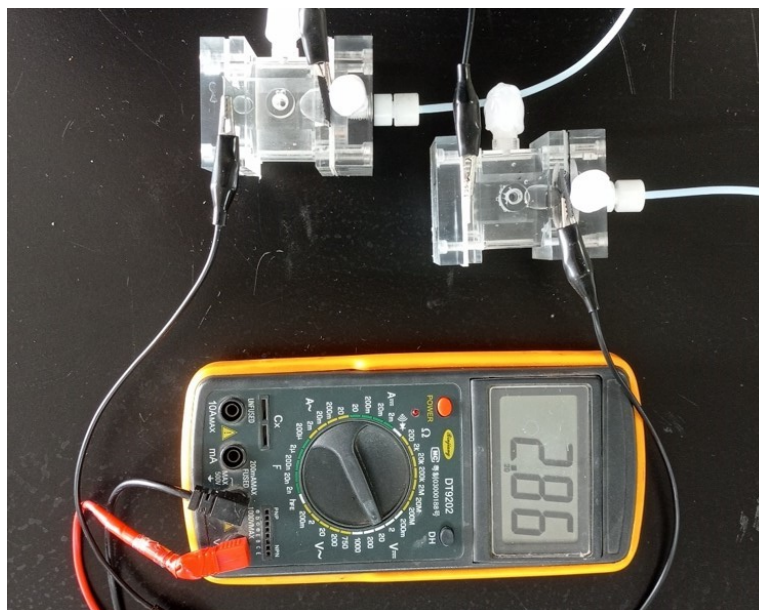
Fig. S22. Open-circuit voltage of the two zinc-air batteries connected in series.
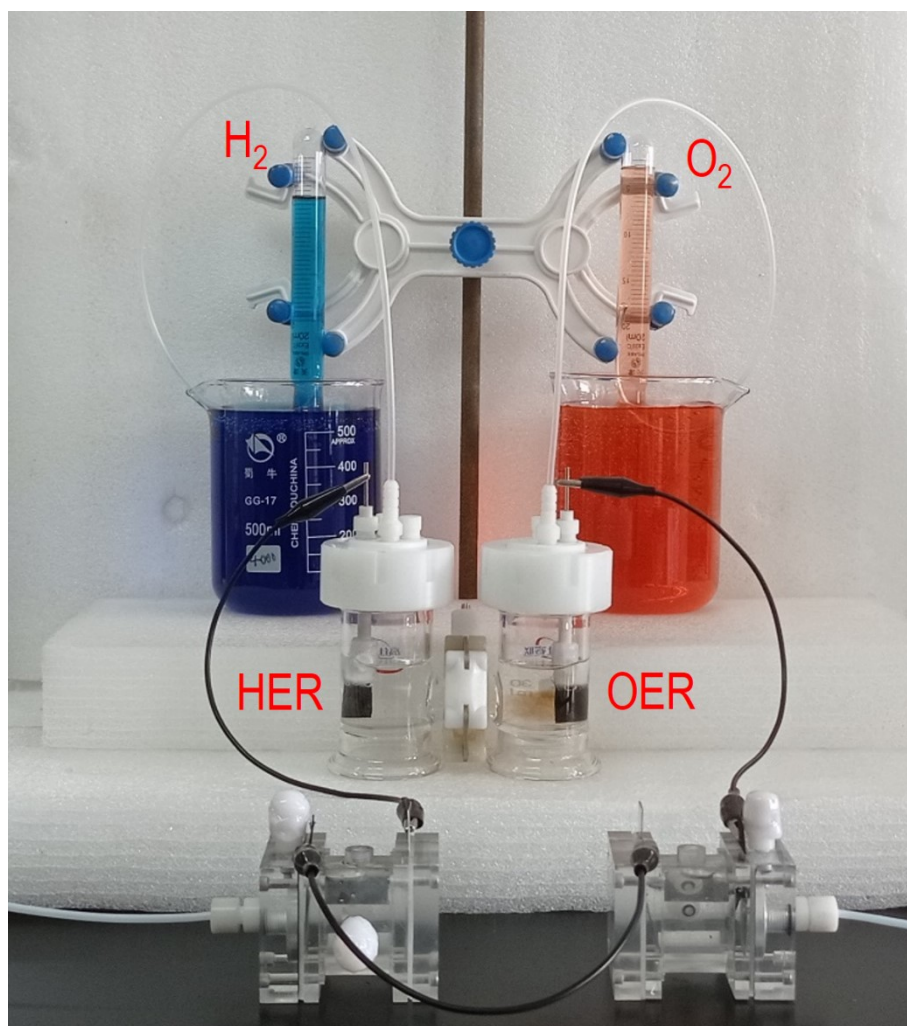
Fig. S23. The enlarged picture of the water displacement instrument.

Fig. S24. Enlarged digital images of the measuring gas quantity generated in 60 min in the two-electrode electrolyzer derived by two zinc-air batteries connected in series.
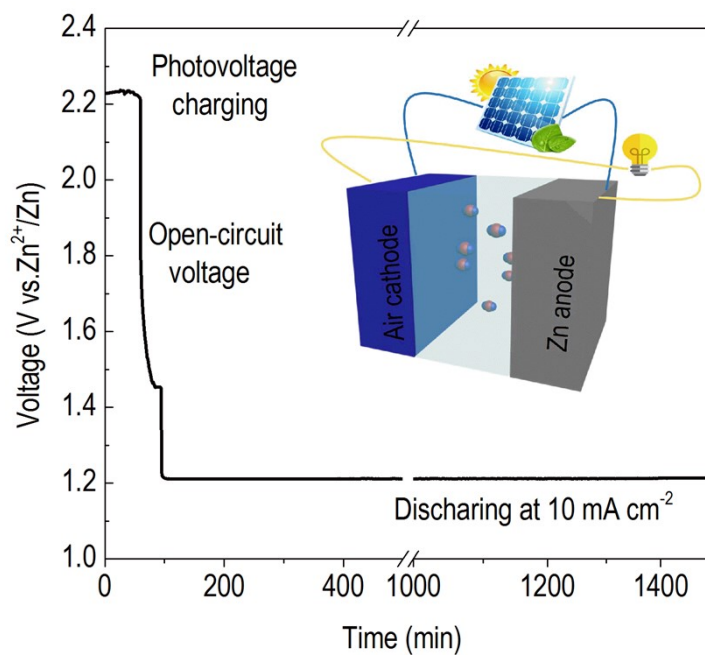
Fig. S25. Photovoltage charging and following discharging plots of the assembled FeNiP@p-NPCF/CC based battery. The inset is the schematic diagram of this photovoltage charging and discharging process.

3. Supplementary tables

Table S1. Performance comparison of FeNiP@p-NPCF/CC and recently reported multifunctional catalysts.

Catalyst	HER		OER		ORR	Reference
	$E_{j=10}$ (mV)	Tafel slope (mV dec^{-1})	$E_{j=10}$ (mV)	Tafel slope (mV dec^{-1})	Half-cell potential ($E_{1/2}$) vs. RHE	
FeNiP/P-NPCF	89	40	317	75	0.82	This work
Fe-Co$_2$P@Fe-N-C	77	56	300	79	0.88	[8]
Fe-N$_4$ SAs/NPC	202	123	430	95	0.885	[9]
FeNi/NPC	260	112	310	62	0.73	[10]
Co$_2$Mn$_1$ LDH	187	60	233	57	0.78	[11]
Co$_2$P/NPG-900	245	108.6	320	66.6	0.81	[12]
CoOx/CoNy@CNz-700	265	84	280	61	0.83	[13]
Co$_4$N@NC-2	283	104	290	67.89	0.84	[14]
Co/CoS/Fe-HSNC	138	110.8	250	62.6	0.906	[15]
CoP@SNC	174	82	350	68	0.79	[16]
Ni@N-HCGHF	95	57	260	63	0.875	[17]
GH-BGQD2	130	95	370	70	0.87	[18]
FeCo/Co2P@NPCF	260	120	330	61	0.79	[19]
CoSA/N,S-HCS	165	95.6	306	38.1	0.85	[20]
CoSA+Co$_9$S$_8$/HCNT	250	101	330	21	0.855	[21]

Table S2. Activity comparison of FeNiP@p-NPCF/CC-catalyzed liquid zinc-air battery and the reported non-precious catalysts.

Catalyst	Peak power density (mW cm^{-2})	Cycling conditions and stability	Ref.
FeNiP@p-NPCF/CC	117	10 mA cm^{-2}, 60 min/cycle for 500 h; no obvious voltage decay	This work.
NCN-1000-80	207	10 mA cm^{-2}, 20 min/cycle for 1000 cycles; no obvious voltage decay	[22]
N-CN9	41	10 mA cm^{-2}, 10 min/cycle for 30 cycles; voltage gap increased ~0.33 V	[23]
Co/CoO@Co-N-C	157	10 mA cm^{-2}, 10 min/cycle for 100 cycles; voltage gap increased ~0.19 V	[24]
NiO/CoN PINWs	80	3 mA cm^{-2}, 10 min/cycle for 50 cycles; voltage gap increased ~0.25 V	[25]
Ni$_3$Fe/N-C	N.A.	10 mA cm^{-2}, 4 h/cycle for 105 cycles; voltage gap increased ~0.20 V	[26]
CoZn-NC-700	152	10 mA cm^{-2}, 10 min/cycle for 385 cycles; voltage gap increased ~0.37 V	[27]
MnO@Co-N/C	130.3	5 mA cm^{-2}, 20 min per cycle for 1900 Cycles (633 h)	[28]
Co$_3$O$_4$/N-rGO	N.A.	3 mA cm^{-2}, 20 min per cycle for 75 cycles (25 h)	[29]
Fe$_{0.5}$Co$_{0.5}$O$_x$/NrGO	86	10 mA cm^{-2}, 2 h per cycle for 60 cycles (120 h)	[30]
Co$_3$FeS$_{1.5}$(OH)$_6$	113.1	2 mA cm^{-2}, 20 min per cycle for 108 cycles (36 h)	[31]
Co$_3$O$_4$/N-CNTAs	N.A.	5 mA cm^{-2}, 10 min per cycle for100 cycles (16.7 h)	[32]
Co-N$_x$-C	152	2 mA cm^{-2}, 20 min per cycle for 180 cycles (60 h)	[33]
C-MOF-C2-900	105	10 mA cm^{-2}, 20 min per cycle for 90 cycles (30 h)	[34]

Table S3. Overall water splitting performance of FeNiP@p-NPCF/CC- and the reported non-precious catalysts-catalyzed electrolyzer.

Catalyst	$E_{J=10}$ (V)	Ref.
FeNiP/NPCS	1.50	This work.
NiFeO$_x$/CNF	1.62	[35]
Ni@N doped graphene	1.60	[36]
MoNi$_4$	1.58	[37]
Fe doped Ni(OH)$_2$	1.64	[38]
NiS	1.61	[39]
NiCoP	1.65	[40]
NiCo$_2$S$_4$	1.63	[41]
Co-P film	> 1.62	[42]
NiSe	1.63	[43]
NiP/Ni	1.62	[44]
NiSe	1.63	[45]
Ni/Mo$_2$C(1:2)-NCNFs	1.64	[46]
NiS	1.64	[47]
NiMo HNRs/Ti mesh	1.64	[48]
NiCo$_2$Px/CNTs	1.61	[49]
Co$_2$P/Mo$_2$C/Mo$_3$Co$_3$C@C	1.74	[50]

4. Supplementary references

[1] B. Mohammadi, S. Pirsa, M. Alizadeh, Preparing chitosan–polyaniline nanocomposite film and examining its mechanical, electrical, and antimicrobial properties, Polymers and Polymer Composites, 27 (2019) 507-517.

[2] B.S. Rathore, N.P.S. Chauhan, M.K. Rawal, S.C. Ameta, R. Ameta, Chitosan–polyaniline–copper(II) oxide hybrid composite for the removal of methyl orange dye, Polym. Bull., 77 (2019) 4833-4850.

[3] Q. Zhou, J. Chen, T. Zhou, J. Shao, In situ polymerization of polyaniline on cotton fabrics with phytic acid as a novel efficient dopant for flame retardancy and conductivity switching, New J. Chem., 44 (2020) 3504-3513.

[4] Y.T. Kang, C.C. Wang, C.Y. Chen, Preparation of 2D leaf-shaped and 3D flower-shaped sandwich-like polyaniline nanocomposites and application on anticorrosion, Journal of Applied Polymer Science, 138 (2020) 49729.

[5] S. Budi, E.P. Rini, M. Paristiowati, A. Imaduddin, D. Syafei, Synthesis and Characterization of High Conductivity Polyaniline Prepared at Room Temperature, Chemistry and Materials, 1 (2022) 7-11.

[6] Y.-P. Zhu, Y.-P. Liu, Z.-Y. Yuan, Biochemistry-inspired direct synthesis of nitrogen and phosphorus dual-doped microporous carbon spheres for enhanced electrocatalysis, Chem. Commun., 52 (2016) 2118-2121.

[7] Y.P. Zhu, Y. Jing, A. Vasileff, T. Heine, S.Z. Qiao, 3D Synergistically Active Carbon Nanofibers for Improved Oxygen Evolution, Adv. Energy Mater., 7 (2017) 1602928.

[8] X.W. Lv, W.S. Xu, W.W. Tian, H.Y. Wang, Z.Y. Yuan, Activity Promotion of Core and Shell in Multifunctional Core–Shell Co2P@ NC Electrocatalyst by Secondary Metal Doping for Water Electrolysis and Zn-Air Batteries, Small, 17 (2021) 2101856.

[9] Y. Pan, S. Liu, K. Sun, X. Chen, B. Wang, K. Wu, X. Cao, W.C. Cheong, R. Shen, A. Han, A bimetallic Zn/Fe polyphthalocyanine-derived single-atom Fe-N4 catalytic site: a superior trifunctional catalyst for overall water splitting and Zn–air batteries, Angew. Chem. Int. Ed., 57 (2018) 8614-8618.

[10] H.X. Zhong, J. Wang, Q. Zhang, F. Meng, D. Bao, T. Liu, X.Y. Yang, Z.W. Chang, J.M. Yan, X.B. Zhang, In Situ Coupling FeM (M= Ni, Co) with Nitrogen-Doped Porous Carbon toward Highly Efficient Trifunctional Electrocatalyst for Overall Water Splitting and Rechargeable Zn–Air Battery, Advanced Sustainable Systems, 1 (2017) 1700020.

[11] K. Li, D. Guo, J. Kang, B. Wei, X. Zhang, Y. Chen, Hierarchical hollow spheres assembled with ultrathin CoMn double hydroxide nanosheets as trifunctional electrocatalyst for overall water splitting and Zn air battery, ACS Sustainable Chemistry & Engineering, 6 (2018) 14641-14651.

[12] Q. Shao, Y. Li, X. Cui, T. Li, H.-g. Wang, Y. Li, Q. Duan, Z. Si, Metallophthalocyanine-based polymer-derived Co2P nanoparticles anchoring on doped graphene as high-efficient trifunctional electrocatalyst for Zn-air batteries and water splitting, ACS Sustainable Chemistry & Engineering, 8 (2020) 6422-6432.

[13] J. Liu, C. Wang, H. Sun, H. Wang, F. Rong, L. He, Y. Lou, S. Zhang, Z. Zhang, M. Du,

CoOx/CoNy nanoparticles encapsulated carbon-nitride nanosheets as an efficiently trifunctional electrocatalyst for overall water splitting and Zn-air battery, Applied Catalysis B: Environmental, 279 (2020) 119407.

[14] H. Ge, G. Li, J. Shen, W. Ma, X. Meng, L. Xu, Co4N nanoparticles encapsulated in N-doped carbon box as tri-functional catalyst for Zn-air battery and overall water splitting, Applied Catalysis B: Environmental, 275 (2020) 119104.

[15] L. Yan, H. Wang, J. Shen, J. Ning, Y. Zhong, Y. Hu, Formation of mesoporous Co/CoS/Metal-NC@ S, N-codoped hairy carbon polyhedrons as an efficient trifunctional electrocatalyst for Zn-air batteries and water splitting, Chemical Engineering Journal, 403 (2021) 126385.

[16] T. Meng, Y.-N. Hao, L. Zheng, M. Cao, Organophosphoric acid-derived CoP quantum dots@ S, N-codoped graphite carbon as a trifunctional electrocatalyst for overall water splitting and Zn–air batteries, Nanoscale, 10 (2018) 14613-14626.

[17] L. Yan, Y. Xu, P. Chen, S. Zhang, H. Jiang, L. Yang, Y. Wang, L. Zhang, J. Shen, X. Zhao, A Freestanding 3D Heterostructure Film Stitched by MOF-Derived Carbon Nanotube Microsphere Superstructure and Reduced Graphene Oxide Sheets: A Superior Multifunctional Electrode for Overall Water Splitting and Zn–Air Batteries, Advanced Materials, 32 (2020) 2003313.

[18] T.V. Tam, S.G. Kang, M.H. Kim, S.G. Lee, S.H. Hur, J.S. Chung, W.M. Choi, Novel graphene hydrogel/B-doped graphene quantum dots composites as trifunctional electrocatalysts for Zn− air batteries and overall water splitting, Advanced Energy Materials, 9 (2019) 1900945.

[19] Q. Shi, Q. Liu, Y. Ma, Z. Fang, Z. Liang, G. Shao, B. Tang, W. Yang, L. Qin, X. Fang, High-performance trifunctional electrocatalysts based on FeCo/Co$_2$P hybrid nanoparticles for zinc–air battery and self-powered overall water splitting, Adv. Energy Mater., 10 (2020) 1903854.

[20] Z. Zhang, X. Zhao, S. Xi, L. Zhang, Z. Chen, Z. Zeng, M. Huang, H. Yang, B. Liu, S.J. Pennycook, Atomically Dispersed Cobalt Trifunctional Electrocatalysts with Tailored Coordination Environment for Flexible Rechargeable Zn–Air Battery and Self-Driven Water Splitting, Advanced Energy Materials, 10 (2020) 2002896.

[21] Y. Li, R. Cao, L. Li, X. Tang, T. Chu, B. Huang, K. Yuan, Y. Chen, Simultaneously integrating single atomic cobalt sites and Co9S8 nanoparticles into hollow carbon nanotubes as trifunctional electrocatalysts for Zn–air batteries to drive water splitting, Small, 16 (2020) 1906735.

[22] H. Jiang, J. Gu, X. Zheng, M. Liu, X. Qiu, L. Wang, W. Li, Z. Chen, X. Ji, J. Li, Defect-rich and ultrathin N doped carbon nanosheets as advanced trifunctional metal-free electrocatalysts for the ORR, OER and HER, Energy Environ. Sci., 12 (2019) 322-333.

[23] C. Zhang, G. Zhang, H. Li, Y. Chang, Z. Chang, J. Liu, X. Sun, Interfacial dehalogenation-enabled hollow N-doped carbon network as bifunctional catalysts for rechargeable Zn-air battery, Electrochim. Acta, 247 (2017) 1044-1051.

[24] X. Zhang, R. Liu, Y. Zang, G. Liu, G. Wang, Y. Zhang, H. Zhang, H. Zhao, Co/CoO nanoparticles immobilized on Co-N-doped carbon as trifunctional electrocatalysts for oxygen reduction, oxygen evolution and hydrogen evolution reactions, Chem. Commun., 52 (2016) 5946-5949.

[25] J. Yin, Y. Li, F. Lv, Q. Fan, Y.Q. Zhao, Q. Zhang, W. Wang, F. Cheng, P. Xi, S. Guo, NiO/CoN

Porous Nanowires as Efficient Bifunctional Catalysts for Zn-Air Batteries, ACS Nano, 11 (2017) 2275-2283.

[26] G. Fu, Z. Cui, Y. Chen, Y. Li, Y. Tang, J.B. Goodenough, Ni_3Fe-N Doped Carbon Sheets as a Bifunctional Electrocatalyst for Air Cathodes, Adv. Energy Mater., 7 (2016) 1601172.

[27] X. Wu, X. Han, X. Ma, W. Zhang, Y. Deng, C. Zhong, W. Hu, Morphology-Controllable Synthesis of Zn-Co-Mixed Sulfide Nanostructures on Carbon Fiber Paper Toward Efficient Rechargeable Zinc-Air Batteries and Water Electrolysis, ACS Appl. Mater. Interfaces, 9 (2017) 12574-12583.

[28] Y. Chen, Y. Guo, H. Cui, Z. Xie, X. Zhang, J. Wei, Z. Zhou, Bifunctional Electrocatalysts of MOF-Derived Co-N/C on Bamboo-Like MnO Nanowires for High-Performance Liquid and Solid-State Zn-Air Batteries, J. Mater. Chem. A, 6 (2018) 9716-9722.

[29] Y. Li, C. Zhong, J. Liu, X. Zeng, S. Qu, X. Han, Y. Deng, W. Hu, J. Lu, Atomically Thin Mesoporous Co_3O_4 Layers Strongly Coupled with N-rGO Nanosheets as High-Performance Bifunctional Catalysts for 1D Knittable Zinc–Air Batteries, Adv. Mater. Interfaces, 30 (2018) 1703657.

[30] L. Wei, H.E. Karahan, S. Zhai, H. Liu, X. Chen, Z. Zhou, Y. Lei, Z. Liu, Y. Chen, Amorphous Bimetallic Oxide–Graphene Hybrids as Bifunctional Oxygen Electrocatalysts for Rechargeable Zn–Air Batteries, Adv. Mater., 29 (2017) 1701410.

[31] H.F. Wang, C. Tang, B. Wang, B.Q. Li, Q. Zhang, Bifunctional Transition Metal Hydroxysulfides: Room-Temperature Sulfurization and Their Applications in Zn–Air Batteries, Adv. Mater., 29 (2017) 1702327.

[32] W. Tian, H. Li, B. Qin, Y. Xu, Y. Hao, Y. Li, G. Zhang, J. Liu, X. Sun, X. Duan, Tuning the wettability of carbon nanotube arrays for efficient bifunctional catalysts and Zn–air batteries, Journal of Materials Chemistry A, 5 (2017) 7103-7110.

[33] C. Tang, B. Wang, H.F. Wang, Q. Zhang, Defect Engineering toward Atomic Co–Nx–C in Hierarchical Graphene for Rechargeable Flexible Solid Zn-Air Batteries, Adv. Mater., 29 (2017) 1703185.

[34] M. Zhang, Q. Dai, H. Zheng, M. Chen, L. Dai, Novel MOF-Derived Co@ N-C Bifunctional Catalysts for Highly Efficient Zn–Air Batteries and Water Splitting, Adv. Mater., 30 (2018) 1705431.

[35] H. Wang, H.-W. Lee, Y. Deng, Z. Lu, P.-C. Hsu, Y. Liu, D. Lin, Y. Cui, Bifunctional non-noble metal oxide nanoparticle electrocatalysts through lithium-induced conversion for overall water splitting, Nat. Commun., 6 (2015) 7261.

[36] Y. Xu, W. Tu, B. Zhang, S. Yin, Y. Huang, M. Kraft, R. Xu, Nickel Nanoparticles Encapsulated in Few‐Layer Nitrogen‐Doped Graphene Derived from Metal–Organic Frameworks as Efficient Bifunctional Electrocatalysts for Overall Water Splitting, Adv. Mater., 29 (2017) 1605957.

[37] Y. Jin, X. Yue, C. Shu, S. Huang, P.K. Shen, Three-dimensional porous MoNi 4 networks constructed by nanosheets as bifunctional electrocatalysts for overall water splitting, Journal of Materials Chemistry A, 5 (2017) 2508-2513.

[38] J.T. Ren, G.G. Yuan, C.C. Weng, L. Chen, Z.Y. Yuan, Uniquely integrated Fe-doped $Ni(OH)_2$ nanosheets for highly efficient oxygen and hydrogen evolution reactions, Nanoscale, 10 (2018) 10620-10628.

[39] J.-T. Ren, Z.-Y. Yuan, Hierarchical Nickel Sulfide Nanosheets Directly Grown on Ni Foam: A Stable and Efficient Electrocatalyst for Water Reduction and Oxidation in Alkaline Medium, ACS Sustainable Chemistry & Engineering, 5 (2017) 7203-7210.

[40] C. Wang, J. Jiang, T. Ding, G. Chen, W. Xu, Q. Yang, Monodisperse Ternary NiCoP Nanostructures as a Bifunctional Electrocatalyst for Both Hydrogen and Oxygen Evolution Reactions with Excellent Performance, Adv. Mater. Interfaces, 3 (2015) 1500454.

[41] A. Sivanantham, P. Ganesan, S. Shanmugam, Hierarchical $NiCo_2S_4$ Nanowire Arrays Supported on Ni Foam: An Efficient and Durable Bifunctional Electrocatalyst for Oxygen and Hydrogen Evolution Reactions, Adv. Funct. Mater., 26 (2016) 4661-4672.

[42] N. Jiang, B. You, M. Sheng, Y. Sun, Electrodeposited Cobalt-Phosphorous-Derived Films as Competent Bifunctional Catalysts for Overall Water Splitting, Angew. Chem. Int. Ed., 54 (2015) 6251-6254.

[43] C. Tang, N. Cheng, Z. Pu, W. Xing, X. Sun, NiSe Nanowire Film Supported on Nickel Foam: An Efficient and Stable 3D Bifunctional Electrode for Full Water Splitting, Angew. Chem. Int. Ed., 54 (2015) 9351-9355.

[44] Y.P. Zhu, Y.P. Liu, T.Z. Ren, Z.Y. Yuan, Self‐Supported Cobalt Phosphide Mesoporous Nanorod Arrays: A Flexible and Bifunctional Electrode for Highly Active Electrocatalytic Water Reduction and Oxidation, Adv. Funct. Mater., 25 (2015) 7337-7347.

[45] C. Tang, N. Cheng, Z. Pu, W. Xing, X. Sun, NiSe nanowire film supported on nickel foam: an efficient and stable 3D bifunctional electrode for full water splitting, Angew. Chem., 127 (2015) 9483-9487.

[46] M. Li, Y. Zhu, H. Wang, C. Wang, N. Pinna, X. Lu, Ni Strongly Coupled with Mo_2C Encapsulated in Nitrogen-Doped Carbon Nanofibers as Robust Bifunctional Catalyst for Overall Water Splitting, Adv. Energy Mater., 9 (2019) 1803185.

[47] W. Zhu, X. Yue, W. Zhang, S. Yu, Y. Zhang, J. Wang, J. Wang, Nickel sulfide microsphere film on Ni foam as an efficient bifunctional electrocatalyst for overall water splitting, Chem. Commun., 52 (2016) 1486-1489.

[48] J. Tian, N. Cheng, Q. Liu, X. Sun, Y. He, A.M. Asiri, Self-supported NiMo hollow nanorod array: an efficient 3D bifunctional catalytic electrode for overall water splitting, J. Mater. Chem. A, 3 (2015) 20056-20059.

[49] C. Huang, T. Ouyang, Y. Zou, N. Li, Z.-Q. Liu, Ultrathin NiCo2Px nanosheets strongly coupled with CNTs as efficient and robust electrocatalysts for overall water splitting, J. Mater. Chem. A, 6 (2018) 7420-7427.

[50] X. Li, X. Wang, J. Zhou, L. Han, C. Sun, Q. Wang, Z. Su, Ternary hybrids as efficient bifunctional electrocatalysts derived from bimetallic metal–organic-frameworks for overall water splitting, J.

Mater. Chem. A, 6 (2018) 5789-5796.